In Vivo Longitudinal Monitoring of Disease Progression in Inflammatory Arthritis Animal Models Using Raman Spectroscopy

Walther, Anders R; Stepula, Elzbieta; Ditzel, Nicholas; Kassem, Moustapha; Bergholt, Mads S; Hedegaard, Martin A B

Published in:
Analytical Chemistry

DOI:
10.1021/acs.analchem.2c04743

Publication date:
2023

Document version:
Final published version

analytical chemistry

pubs.acs.org/ac

Article

In Vivo Longitudinal Monitoring of Disease Progression in Inflammatory Arthritis Animal Models Using Raman Spectroscopy

Anders R. Walther, Elzbieta Stepula, Nicholas Ditzel, Moustapha Kassem, Mads S. Bergholt,* and Martin A. B. Hedegaard*

Cite This: *Anal. Chem.* 2023, 95, 3720−3728

Read Online

ACCESS | Metrics & More | Article Recommendations | Supporting Information

ABSTRACT: Current techniques for monitoring disease progression and testing drug efficacy in animal models of inflammatory arthritis are either destructive, time-consuming, subjective, or require ionizing radiation. To accommodate this, we have developed a non-invasive and label-free optical system based on Raman spectroscopy for monitoring tissue alterations in rodent models of arthritis at the biomolecular level. To test different sampling geometries, the system was designed to collect both transmission and reflection mode spectra. Mice with collagen antibody-induced arthritis and controls were subject to *in vivo* Raman spectroscopy at the tibiotarsal joint every 3 days for 14 days. Raman-derived measures of bone content correlated well with micro-computed tomography bone mineral densities. This allowed for time-resolved quantitation of bone densities, which indicated gradual bone erosion in mice with arthritis. Inflammatory pannus formation, bone erosion, and bone marrow inflammation were confirmed by histological analysis. In addition, using library-based spectral decomposition, we quantified the progression of bone and soft tissue components. In general, the tissue components followed significantly different tendencies in mice developing arthritis compared to the control group in line with the histological analysis. In total, this demonstrates Raman spectroscopy as a versatile technique for monitoring alterations to both mineralized and soft tissues simultaneously in rodent models of musculoskeletal disorders. Furthermore, the technique presented herein allows for objective repeated within-animal measurements potentially refining and reducing the use of animals in research while improving the development of novel antiarthritic therapeutics.

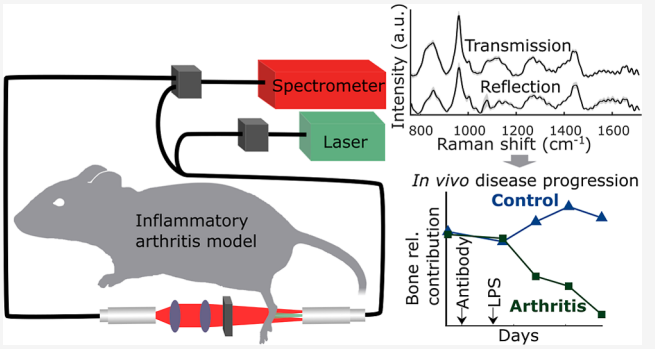

Rheumatoid arthritis (RA) is a chronic inflammatory autoimmune disorder characterized by synovial inflammation and formation of pannus, which leads to the destruction of local articular structure, bone erosion, and functional disabilities.[1,2] A variety of longitudinal animal models that closely resemble the characteristic features found in patients with inflammatory arthritis are currently studied to elucidate on the complex pathogenic mechanisms and to validate novel therapeutic approaches.[3−5] Common models of inflammatory arthritis in rodents are collagen-induced arthritis (CIA), collagen antibody-induced arthritis (CAIA), human tumor necrosis factor transgenic (hTNF-Tg) mice, and rat pristane-induced arthritis (PIA).[5] As the pathogenic features of these models all are reminiscent to some degree of human arthritis,[3,4,6] they are potentially associated with pain, discomfort, and distress for the animals.[7] The severity and degree of arthritis in rodent models can be assessed by a variety of methods. Tests can be routine or specialized, invasive or non-invasive, and performed before or after euthanasia.[4] Recording body weight and hind paw swelling using plethysmography, calipers, or clinical scoring is non-invasive and relatively straightforward to perform; however, these are only indirect measures of disease progression. In addition, semi-quantitative scoring techniques are challenged by their subjective nature.[8] Importantly, none of these techniques offer any biomolecular information. Blood samples can be collected in a minimally invasive manner for the assessment of serum biomarkers, but this is not recommended solely for this purpose.[7] Histopathology is the gold standard, providing the most detailed cellular and molecular characterization of a disease; however, it is inherently destructive and requires the sacrifice of several animals for longitudinal studies.[9] Evaluating bone mineral density using dual X-ray absorptiometry (DXA) can be routinely applied post-mortem, whereas imaging modalities such as conventional radiography,[10] micro-computed tomography (μCT), and magnetic resonance imaging

Received: October 27, 2022
Accepted: January 23, 2023
Published: February 9, 2023

https://doi.org/10.1021/acs.analchem.2c04743
Anal. Chem. 2023, 95, 3720−3728

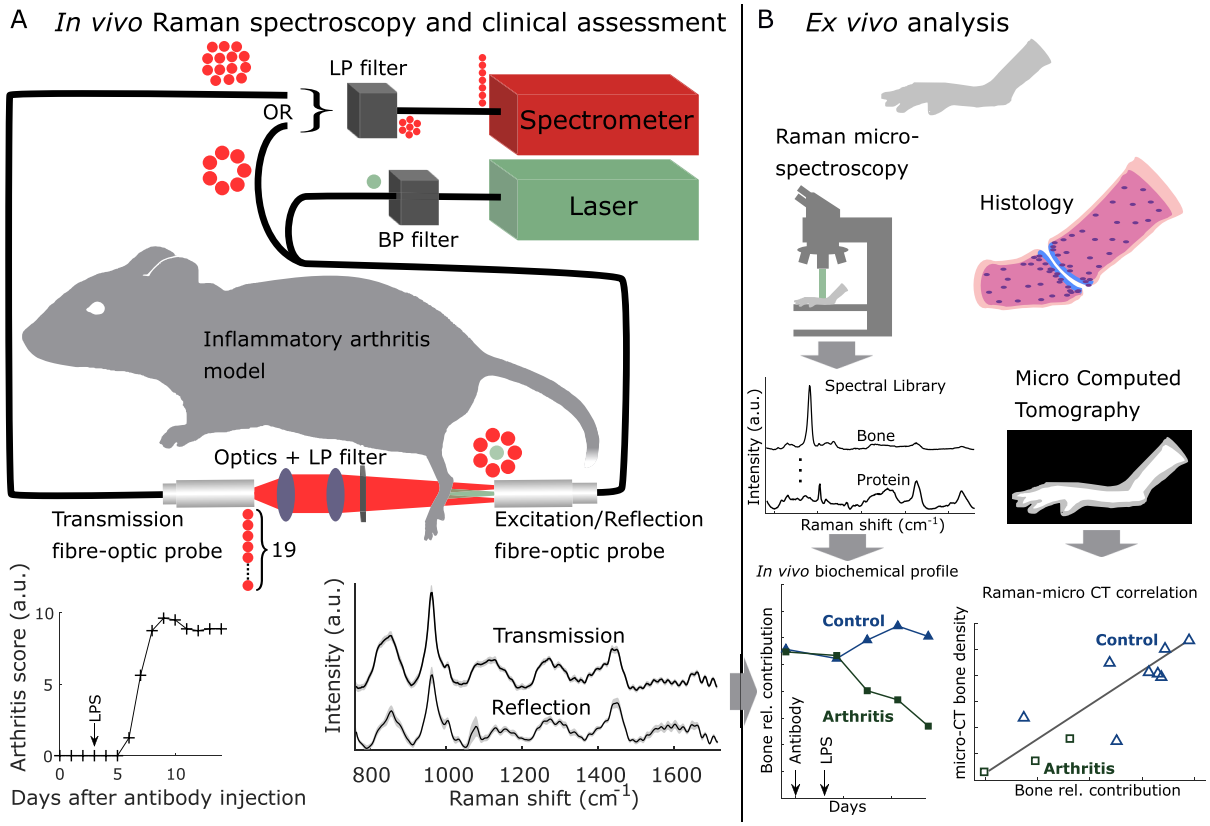

Figure 1. Conceptual illustration of the experimental workflow. (A) *In vivo* Raman spectroscopy system for monitoring disease progression in rodent models of inflammatory arthritis and (B) *ex vivo* analysis for determination of biochemical disease progression profile and correlation of spectral features with histology and μCT. Collagen antibody (antibody); lipopolysaccharide (LPS).

(MRI)[11] belong to the more specialized, time-consuming, and expensive techniques.[4,9,12] These can be applied *ex vivo* and *in vivo*, providing structural information at high spatial resolution, however, with limited biochemical information. In addition, the use of ionizing radiation may be a limitation in longitudinal studies. Therefore, there is an unmet need for non-invasive tools capable of temporal characterization of morphological and molecular alterations in repeated within animal measurements *in vivo*, providing a means to reduce the number of experimental animals.[9]

Raman spectroscopy (RS) is a non-invasive, non-destructive, optical technique based on the inelastic scattering of light by molecules.[13] In the context of biomedical applications, RS can provide insight into the composition of samples, as proteins, RNA/DNA, lipids, carbohydrates, and so forth produce different Raman spectra. This allows for the detection of changes in the relative concentration of such components in tissue as a result of pathological conditions.[13−21] With the development of miniaturized fiber-optic probes,[22] it is possible to apply RS *in vivo*/*in situ*.[15,16,19,23−25]

Together, this motivates the use of RS in animal experiments involving musculoskeletal diseases, as biochemical alterations in joints and limbs can be assessed non-invasively and repeatedly using non-ionizing radiation.

Here, we demonstrate the *in vivo* assessment of biomolecular tissue alterations in an inflammatory arthritis mouse model using a transflection Raman setup. We developed an experimental workflow constituting *in vivo* spectral and clinical assessment of hindlimbs and *ex vivo* analyses (Figure 1). The system was employed for non-invasive acquisition of Raman spectra of tibiotarsal joints in both transmission and reflection type measurements. First, we longitudinally characterized and investigated the *in vivo* spectra. Second, we compared histological analysis and *ex vivo* μCT bone densities at the tibiotarsal joint with Raman-derived measures of bone content, producing longitudinal profiles of bone densities based on the *in vivo* spectra. Third, using a spectral library of tissue components, we quantified the content of additional major tissue components during disease. Altogether, this provides the foundation for non-invasive monitoring of disease progression in models of inflammatory arthritis, potentially leading to a reduction and refinement in the use of animals and improving the development of novel therapeutic agents within the fields of bone and joint disorders.

EXPERIMENTAL SECTION

Ethics and Approval. All *in vivo* experiments were performed under the permission from the National Danish Animal Experiments Inspectorate (permission number 2020-15-0201-00682). Danish regulations for the care and use of laboratory animals were maintained throughout the experiment period. Experiments complied with European legislation and associated guidelines for animal experiments. ARRIVE guidelines for animal experiments were followed.[26]

Animals and Collagen Antibody-Induced Arthritis. Inflammatory arthritis was induced[6,27] in 2 month old, female C57BL/6 mice (n = 8, Taconic Denmark) by intraperitoneal injection (IP) of 5 mg collagen antibodies (500 μl solution) on day 0, followed by IP injection of 50 μg lipopolysaccharide (100 μl solution) on day 3 according to the description of the

https://doi.org/10.1021/acs.analchem.2c04743
Anal. Chem. 2023, 95, 3720−3728

manufacturer (Arthrogen-CIA 5 clone Cocktail Kit, Chondrex). Controls (n = 8) received 500 and 100 μl saline by IP injection on day 0 and 3, respectively. The mice were randomly assigned to CAIA and controls. The 16 mice were kept in groups of four in four cages with a soft bedding material and fed ad libitum. The mice were sacrificed 14 days after arthritis induction, and the hindlimbs were excised, fixed in 10% neutral buffered formalin (4% formaldehyde) for 2 days at room temperature, and transferred to saline solution for storage at 4 °C.

Clinical Evaluation of Arthritis. Mice were examined daily from day 0 to obtain an arthritis score based on the number of inflamed joints. In this scoring system, each inflamed toe or knuckle gave 1 point, whereas an inflamed wrist or ankle gave 5 points, resulting in a score of 0−15 (five toes + five knuckles + one wrist/ankle) for each paw and 0−60 points for each mouse.[28]

Transflection Raman Spectroscopy System. The *in vivo* in-house built RS system is depicted in Figure 1A. The system consists of a near-infrared (NIR) multimode diode laser emitting at a wavelength of 785 nm (B&W Tek Inc.), a series of optical multimode, low OH fibers, filters (Semrock), fiber-collimators (Thorlabs), and lenses (Thorlabs). Band-pass (BP) and long-pass (LP) filters were utilized to suppress laser spectral impurities, silica background signals from fiber-optics, and Rayleigh scattered light. A filtered Raman volume probe (EM Vision LLC), fiber-coupled (100 μm core, Thorlabs) to the laser through a BP filter/double collimator assembly, delivered the excitation light to the hindlimb of the mice through a central excitation fiber and collected Raman backscattered light (reflection mode) through seven, 300 μm core, encircling fibers. This probe contained both BP and LP filters at the probe tip. The Raman backscattered light collected by the probe was directed through an LP filter/double collimator assembly before being fiber-coupled (round-to-line fiber bundle, Thorlabs) to the spectrometer (20 μm slit, Raman Eagle S, Ibsen Photonics) equipped with a charge-coupled device (CCD, 2000 × 256 pixels, 15 × 15 μm pixel size), (iVAC, Andor Oxford Instruments). Forward Raman scattered light (transmission mode) was collected by projecting the image of a 19 line-to-round, 100 μm core, fiber bundle (Andor Oxford Instruments) onto the front of the mouse hindlimb using a 19 mm and a 40 mm focal length, B-coated achromatic doublet (Thorlabs). A LP filter was positioned between the mouse limb and lens assembly. Raman forward and back scattered light were collected sequentially by manually changing the input to the LP filter assembly leading to the spectrometer. Fiber probes and lenses were mounted using a 30 mm cage system (Thorlabs). The mouse was placed on top of the system on a customized 3D-printed bed, which allowed one hindlimb to be placed in the optical axis. All Raman measurements were performed using an in-house developed graphical user interface written in the MATLAB programming environment (version R2017a, Mathworks Inc.) utilizing functions from the Andor software development kit (Andor, Oxford Instruments). The spectrometer CCD was configured to operate at −65 °C with a horizontal readout rate of 0.13 MHz and a preamp gain of 2.

Longitudinal Raman Spectroscopy of Live Animals. Raman transmission and reflection spectra were collected from both hindlimbs of all 16 mice one day prior to the administration of antibodies (Raman baseline, day −1) and on day 4, 7, 10, and 13 to resolve the disease progression while minimizing animal handling. Both transmission and reflection Raman spectra were collected by illuminating the area at the calcaneus. The 19 collection fibers used for transmission mode measurements were projected onto the mouse hindlimb, spanning a line (5 mm) across the tibiotarsal joint to the metatarsal region. All *in vivo* spectra spanning the spectral range 0−3600 cm^{-1} (<240 cm^{-1} effectively attenuated by LP filters) were collected using full vertical binning of the CCD, 60 s acquisition time, and two accumulations for each measurement. Both accumulations were stored, allowing for efficient cosmic ray removal during data processing (see Supporting Information). A total laser power of ∼20 mW with a laser spot size of ∼1.5 mm (1/e^2) at the hindlimb was used, resulting in an approximate intensity of 1 W/cm^2. The laser spot size was determined using the knife-edge technique.[29] Similar intensities, using a laser emitting at a wavelength of 789 nm, have previously been shown to produce a mild increase in temperature in human and chicken skin (∼1 °C at a skin depth of 0.5 mm).[30] We did not observe any visible effects on the skin at the area of exposure during the experiment. Raman measurements were performed in the dark chamber of an IVIS Spectrum *In Vivo* Imaging System (PerkinElmer). The mice were anesthetized using 2% isoflurane in pure oxygen during Raman spectroscopy. Reflection and transmission spectra of a polystyrene reference sample (Bruker) were collected (∼50 mW laser power, 5 s acquisition time, and 2 accumulations) on each day of Raman measurement and used to check for spectral drift.

Raman Micro-spectroscopy. Raman micro-spectroscopy of *ex vivo*, fixed, left-side hindlimbs was conducted with an in-house built confocal Raman imaging setup (details in Supporting Information). Five spectra were collected using 5−10 s acquisition time and 60 mW laser power at the sample at five different locations and averaged for each tissue component. The fixed tissues were trimmed and polished with a scalpel and rotary tool prior to micro-spectroscopy to expose the desired tissue parts, producing a spectral library of bone, lipids, muscle, skin, and tendon from five control mice and pannus spectra from a mouse with arthritis.

Spectral Data Processing. All spectral processing and analyses were performed in MATLAB (version R2022a, Mathworks Inc.). Spectra from live animals and library spectra were subject to baseline correction,[31,32] cosmic ray removal,[33] smoothing, and normalization (details in Supporting Information). Spectra collected in reflection were also subject to subtraction of the fiber-optic probe background spectrum. Spectral analysis was performed in the fingerprint wavenumber range 760−1720 cm^{-1} due to impairing tissue autofluorescence and diminishing signal outside this region. Mineral-to-matrix ratios[34] (MTMRs) were calculated by extracting the area of the phosphate symmetric stretch band of hydroxyapatite at 960 cm^{-1} using a single Gaussian profile fit and dividing this by the area of the amide I band in the range 1560−1700 cm^{-1}.

Constrained Library-Based Spectral Decomposition. Pre-processed spectral observations acquired *in vivo* were modeled by a linear combination of library spectra representing pure biochemical components.[35,36] This allowed for estimating the relative contributions of biochemically distinct tissue constituents. The modeling was performed using a non-negative least-squares fitting algorithm in MATLAB. Relative spectral contributions were subject to the closure constraint (their sum equal to 1). The spectral library was

https://doi.org/10.1021/acs.analchem.2c04743
Anal. Chem. 2023, 95, 3720−3728

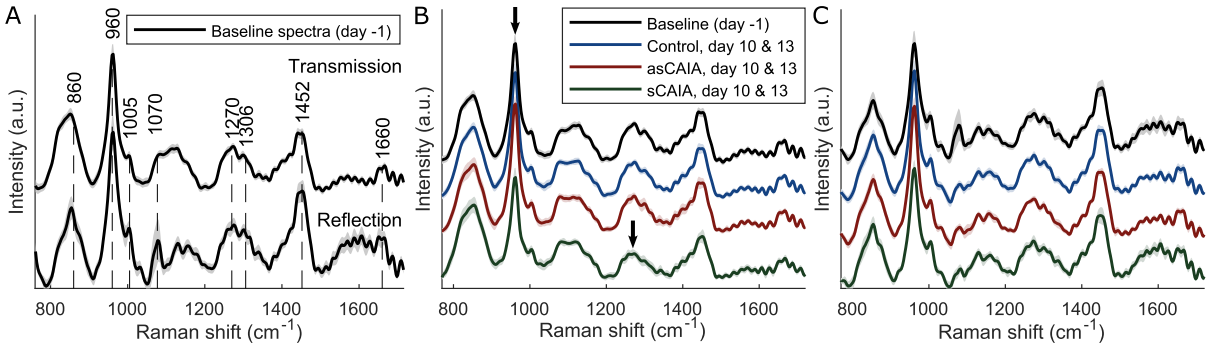

Figure 2. *In vivo* Raman spectroscopy. (A) Average of all hindlimb transmission and reflection spectra collected at day −1 (baseline). CAIA mice were divided into groups of asymptomatic CAIA (asCAIA) and symptomatic CAIA (sCAIA) according to zero or none-zero hindlimb clinical score, respectively. Comparison of transmission (B) and reflection (C) average baseline spectra with control, asymptomatic CAIA (asCAIA), and symptomatic CAIA (sCAIA) spectra collected at days 10 and 13. Average (solid line) ± standard deviation (shaded region). Arrows indicate the position of the clearest spectral differences between the control, asCAIA, and sCAIA average transmission spectra.

composed of the spectra collected from *ex vivo* fixed mouse hindlimbs using Raman micro-spectroscopy.

μCT and Histology. μCT was performed on 16 right-side fixed hindlimbs with a high-resolution μCT system (vivaCT40, Scanco Medical). Volumetric bone mineral density (vBMD) was determined from the 3D reconstructions. Upon completing μCT measurements, the 16 right-side hindlimbs were processed for histological analysis. μCT images of the left-side distal tibia and entire foot for visualizing bone remodeling were captured using a Scanco μCT50 (Scanco Medical). For details on μCT and histology, see Supporting Information.

Regression Analysis. Regression analysis between μCT vBMDs (response variable) and Raman-derived mineral-to-matrix ratios (predictor variable) was performed by linear regression for reflection Raman measurements.

Multivariate partial least-squares (PLS) regression for transmission Raman measurements was performed using MATLABs built in PLS algorithm, with the entire Raman spectrum as a predictor variable and using two components. The algorithm applies mean-centering of the spectral observations. Determination of model complexity and performance was evaluated using leave-one-out cross validation.

RESULTS AND DISCUSSION

Biomolecular Assessment of Disease Progression *In Vivo*. The onset of arthritis in CAIA mice was observed at day 6, and a maximum incidence of 50% was retained from day 7, while no control mice developed arthritis (Supporting Information, Figure S1). Arthritis severity in CAIA mice was mild and peaked on day 9. Only the hindlimbs showed clinical symptoms by swelling of the ankle and knuckles, with little to no effect on the distal toe joints. Average Raman spectra ±1 standard deviation (SD) of mouse hindlimbs collected in transmission and reflection mode one day prior to administration of antibodies (Figure 2A) showed typical spectral features related to bone and soft tissue components. Intense bands were found at 860, 960, 1200−1350, 1452, and 1520−1720 cm^{-1}. These bands correspond to proline/hydroxyproline, hydroxyapatite, amide III, CH_2-deformation, and amide I, respectively. The amide I region was of relatively poor quality due to high tissue autofluorescence and spectrometer etalon effects. The sharp minor peaks at 1005 and 1070 cm^{-1} in the transmission and reflection baseline spectra are related to phenylalanine,[37,38] and lipids/apatite, respectively.[34,39] In the amide III region, a sharp feature was found at 1270 cm^{-1} which gains contributions from both alpha helix proteins and lipids,[37,40] while the 1306 cm^{-1} peak also gains contribution from lipids.[39,40] In general, the baseline spectra resembled those of musculoskeletal tissue, that is, adipose tissue[41] and bone matrix.[34,36] The bone mineral band at 960 cm^{-1} was relatively low in the reflection measurements as compared to the transmission. Such differences were to be expected due to the different collection geometries. In reflection mode, the collected Raman signal originated primarily from the region of excitation[42] that is calcaneus. This collection geometry also gains a high contribution from Raman signals generated in the skin. In transmission, the collection geometry is essentially a special case of spatially offset Raman spectroscopy (SORS)[43] which favors the collection of Raman signals originating from deeper regions of the sample. In SORS, the sampling volume is relatively large compared to conventional techniques using a backscattering geometry. In addition, we collected Raman signals from a 5 mm line of fibers projected onto the hindlimb in the direction along the tibia and foot. As a result, the transmission spectra represented a variety of deep anatomical locations across the tibiotarsal joint. To investigate spectral changes associated with disease activity for different timepoints, the spectral dataset from CAIA mouse hindlimbs was divided into asymptomatic CAIA (asCAIA, $n = 9$) and symptomatic CAIA (sCAIA, $n = 7$), according to zero or non-zero limb clinical score, respectively. At each timepoint, the control group consisted of $n = 16$ spectral observations. By comparison, the average transmission spectrum of sCAIA, day 10 and 13 showed dissimilarities with the average baseline spectrum (Figure 2B). This is mostly manifested as a loss of intensity in the mineral band at 960 cm^{-1} and changes in the amide III region. Changes in the mineral band could indicate bone erosion, which along with inflammation, loss of proteoglycans, cartilage degradation, and pannus formation, is a typical feature of RA.[5,6,44] Relative contributions to the amide III band have previously been linked to protein secondary structure with beta sheet and random coil contributing mainly to the region below 1240 cm^{-1} and alpha helix to the region above 1260 cm^{-1}.[37] We speculate that the observed changes in the amide III band for sCAIA mice could be due to an increase in inflammatory cells in the synovium and loss of cartilage and organic bone matrix; however, the exact mechanism remains open to further investigation. In contrast, both the average spectra of control

https://doi.org/10.1021/acs.analchem.2c04743
Anal. Chem. 2023, 95, 3720−3728

and asCAIA, day 10 and 13 were more similar to the average baseline spectrum. In reflection, it was difficult to directly observe differences based on the average spectra (Figure 2C). Thus, to extract more detailed information of disease progression from *in vivo* Raman spectra, we collected a range of library spectra (Figure 3A) representing pure tissue components from *ex vivo* hindlimbs of control mice using Raman micro-spectroscopy. Following this, every *in vivo* observation was modeled as a linear combination of the library spectra. The tissue components that produced sufficiently close fits to the measured spectra (Figure 3B) consisted of bone, tendon, skin, muscle, and lipids. This approach allowed for both estimating the amide I spectral region, often used as a measure of protein content, and for estimating relative contributions from pure tissue components given by the modeling coefficients.

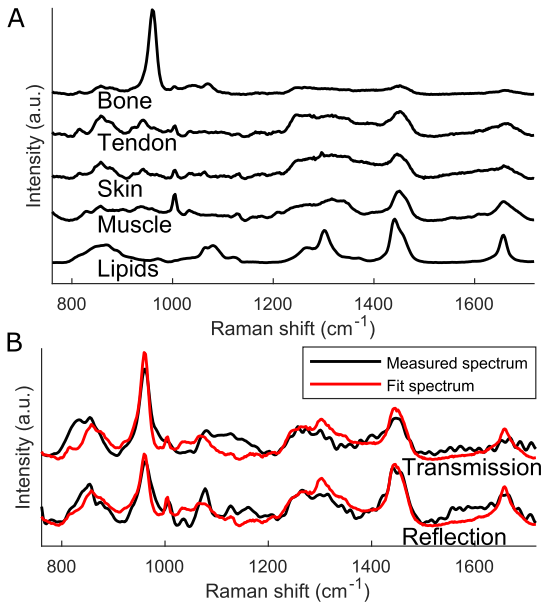

Figure 3. Spectral library and fitting. (A) Library composed of spectra collected *ex vivo* from hindlimbs of control mice using micro-spectroscopy (lipids, muscle, skin, tendon, bone). (B) Examples of library-based spectral decomposition fits to *in vivo* measured spectra.

Histological Analysis and μCT. Histological analysis of hindlimbs revealed a high similarity between the control group and mice that received collagen antibody treatment and later showed absence of clinical symptoms of inflammation (Figure S2). In contrast, hindlimbs from mice that exhibited symptoms of arthritis (sCAIA) revealed a pronounced synovial pannus formation, bone erosion, and bone marrow inflammation. This supports the observed spectral similarities between mice from the control group and asCAIA and their dissimilarity with sCAIA mice.

The lower mineral content of bone in sCAIA mice was reflected by μCT 3D reconstructions showing clear bone remodeling in sCAIA mice and none for both asCAIA and controls (Figure S3). In general, the histological and μCT analysis suggested a reduction in bone mass, suppression of both subcutaneous lipid pockets, and bone marrow adipose tissue, which were instead replaced by proteinaceous and highly cellularized pannus for sCAIA mice. We, therefore, investigated whether these observations were reflected in the Raman spectra acquired *in vivo*. A common spectral measure of bone mineral content is the mineral-to-matrix ratio (MTMR).[34]

Mineral-to-Matrix Ratio and Bone Mineral Density. Computing the MTMR for all *in vivo* spectra indicated a significant decrease (Kruskal–Wallis $***p < 0.001$, Dunnett's multiple comparison $***p < 0.01$) in the mineral content relative to proteinaceous tissue components for both reflection and transmission spectral observations of hindlimbs exhibiting clinical symptoms (Figure S4A). In both cases, the MTMRs of control and asCAIA were not significantly different. In addition, the MTMR of *in vivo* reflection measurements at day 13 correlated well with the corresponding μCT-derived vBMD (Figure S4B). This correlation was lower for the transmission measurements, which may indicate that the sampling volume of reflection mode measurements coincided better with the region of interest used for estimating vBMD. The sCAIA group showed the lowest vBMD values compared to asCAIA and control mice (Figure S4B), indicating the presence of arthritis-induced bone erosion. It should be noted that vBMD only accounts for the remaining bone and does not provide any information on the total bone loss.

To demonstrate the concept of monitoring disease activity, we produced time-resolved retrospective predictions of vBMD

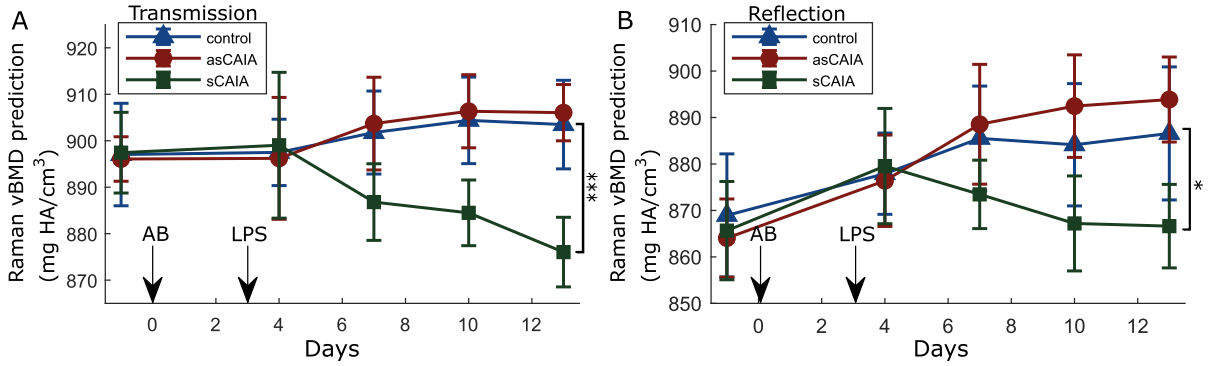

Figure 4. Raman volumetric bone mineral density predictions. Retrospective Raman predictions of vBMD in transmission (A) and reflection (B) demonstrating the concept of monitoring disease progression. Averages (markers) ± standard deviations (error bars). Arrows indicate timepoints for collagen antibodies (AB) and lipopolysaccharide (LPS) injections in CAIA mice. In (A) and (B), data were divided into control ($n = 16$), asCAIA ($n = 9$), and sCAIA ($n = 7$) for each timepoint. Kruskal–Wallis test and Dunnett's multiple comparisons with the control group, $*p < 0.05$, $***p < 0.001$.

https://doi.org/10.1021/acs.analchem.2c04743
Anal. Chem. 2023, 95, 3720−3728

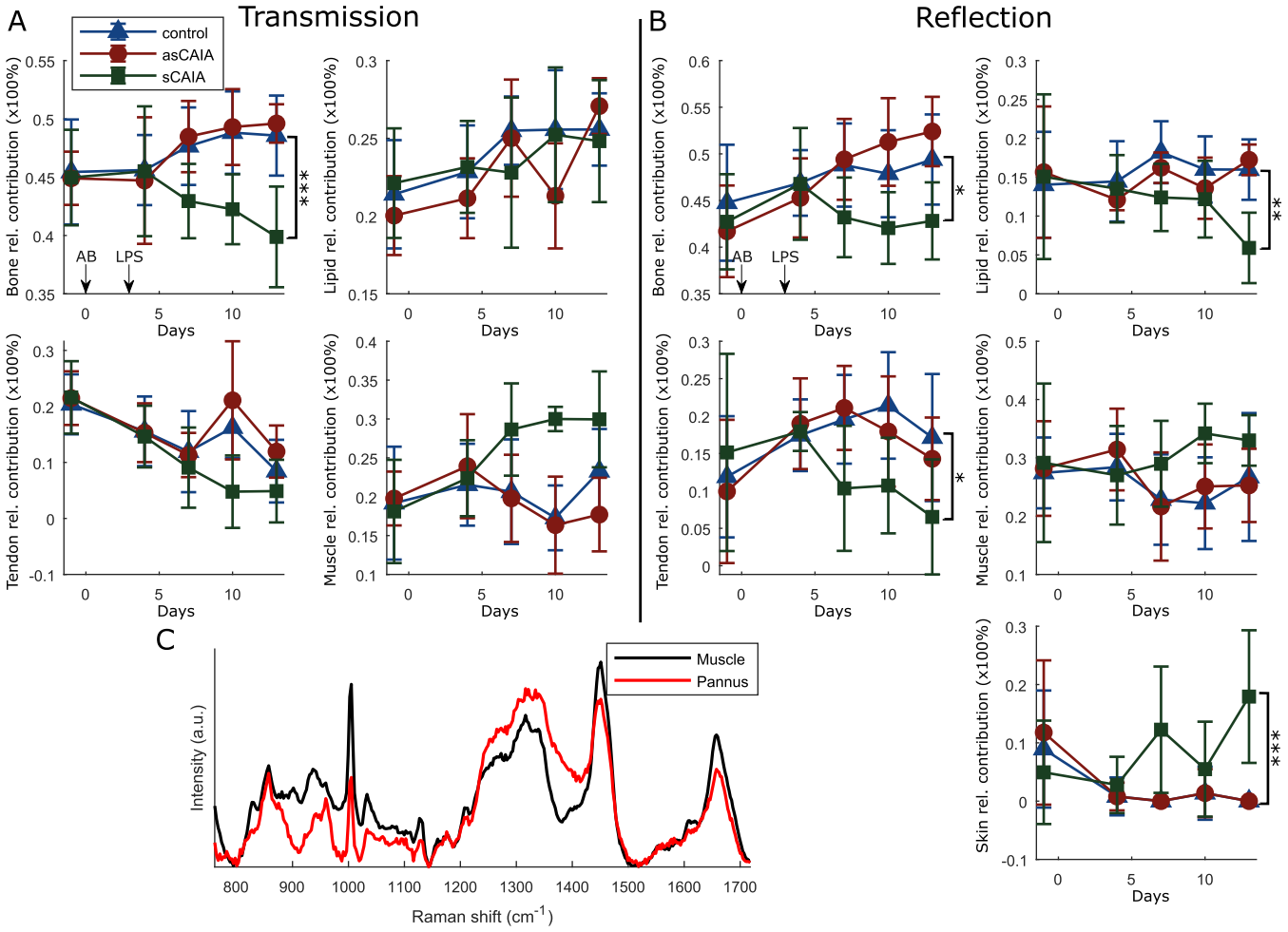

Figure 5. Tissue component dynamics from library-based spectral decomposition of *in vivo* Raman spectra. (A) Decomposition of transmission spectra using a spectral library of bone, lipids, tendon, and muscle. (B) Decomposition of reflection spectra using a spectral library of bone, lipids, tendon, muscle, and skin. Data are presented as the average relative contribution (data points) and standard deviation (error bars) for control (n = 16 spectra), asymptomatic CAIA (asCAIA, n = 9 spectra), and symptomatic CAIA (sCAIA, n = 7 spectra) mice at each timepoint. Significant difference between groups at day 13 is indicated by the Kruskal–Wallis test, $p < 0.01$, and Dunnett's multiple comparisons with control group, $^{*}p < 0.05$, $^{**}p < 0.01$, $^{***}p < 0.001$. Arrows indicate the timepoint for collagen antibodies (AB) and lipopolysaccharide (LPS) injections in CAIA mice. (C) Comparison of muscle library spectrum and pannus spectrum collected *ex vivo* from the sCAIA mouse hindlimb.

from Raman-derived features (Figure 4). Due to the relatively high correlation between μCT vBMD and MTMR from reflection mode, day 13 measurements, we developed a linear regression model for the retrospective conversion of MTMRs into vBMD predictions (Figure S4D). For transmission mode measurements, we applied a two-component partial least squares (PLS) regression (Figure S4C) using the entire Raman spectrum as a predictor variable, as the MTMR alone did not exhibit a sufficiently high correlation to vBMD. This approach significantly improved the vBMD predictions, producing a model with performance (R^2 = 0.8). The PLS approach takes advantage of the more complex spectral variations found in the transmission measurements to predict vBMDs however can, unlike linear regression, easily be subject to overfitting. The retrospective predictions of vBMDs (Figure 4A,B) follow the same trend for all groups until the onset of disease, observed clinically at day 6, in the sCAIA group. Then, for both reflection and transmission measurements, the predicted vBMDs drop in the sCAIA group, while controls and asCAIA mice follow similar trends throughout the experiment. Statistical analysis of day 13 vBMD predictions showed a significant difference between the control and sCAIA groups (Kruskal–Wallis test reflection: $p < 0.01$; transmission $p < 0.001$, Dunnett's test reflection: $p < 0.05$; transmission: $p < 0.001$). This was not the case for controls and asCAIA. Predictions from reflection measurements indicate an increase in vBMD over the entire course of the experiment for controls and asCAIA mice. Whether this is due to continuous bone development in the mice is unknown. However, the bone structure of the murine tibia and tarsus has previously been shown to change as a function of age.[16,45−47] Together, the results demonstrate the use of RS for the determination of mineral content in calcified tissue during disease progression in rodents, providing a means of extracting information on vBMD repeatedly on the same animals without risking the effects associated with ionizing radiation. Monitoring of bone mineral density is an important tool in *in vivo* efficacy studies of antiarthritic therapeutics.[4] However, both soft tissue changes and bone deterioration can be observed using histology and MRI at different timepoints during the disease progression and even prior to loss of bone mineral density, depending on specific models and conditions.[11,48] While histology remains

https://doi.org/10.1021/acs.analchem.2c04743
Anal. Chem. 2023, 95, 3720−3728

the gold standard for assessing alterations to soft tissue, it is inherently destructive and therefore impractical for longitudinal studies. On the contrary, the spectroscopic technique presented herein can provide molecular information related to soft tissue non-destructively, albeit without spatial information.

Progression of Tissue Components by Spectral Library-Based Fitting. The major changes to tissue components induced by inflammatory arthritis were associated with the loss of adipose tissue and bone along with an increase in the proteinaceous inflammatory matrix, as indicated by the histological analysis.

Lipids and proteins have highly overlapping spectral bands of typically much lower intensity and signal-to-noise ratio than the phosphate band (~960 cm^{-1}) of bone apatite. Thus, fitting single lipid and protein bands to extract their relative contribution to the overall spectrum, as when estimating MTMRs, is not feasible. Instead, the multivariate, spectral library-based fitting method was used to estimate relative tissue component contributions and dynamics (Figure 5). The average trend for bone matrix (Figure 5A,B) resembles those of Raman's predicted vBMD (Figure 4A,B) with striking similarity in both reflection and transmission. In both cases, sCAIA mice show a time-dependent degradation of bone. For most components encompassed by the spectral library (Figure 3A), the sCAIA group showed tissue dynamics different from the asCAIA and control groups, which, in contrast, followed similar tendencies. In reflection, the contribution from lipids and tendon generally decreased over time for sCAIA mice and was significantly lower than the control group by day 13. These results are in line with the histological analysis, which qualitatively suggested suppression of lipids and pannus formation in the joints for sCAIA mice. In transmission, the tendon signal also decreased the most for the sCAIA group, however, it was not significantly different from the control group by day 13. In addition, the contribution from lipids followed the same trend for all groups. Whether the contribution from the tendon decreased because of the developing pannus limiting retrieval of the tendon signal or due to tendon molecular changes associated with inflammation is unknown. A clear increase (not significant at day 13) in contribution from muscle-like tissue for sCAIA was observed in transmission measurements (Figure 5A). Similarly, in reflection, the contribution from muscle for the sCAIA group followed a different trend compared to the control and asCAIA groups. In addition, reflection mode measurements showed an increase in skin contribution for the sCAIA group (Figure 5B), which was significantly different from the control group at day 13. In transmission, the contribution from skin remained zero at all timepoints (data not shown), suggesting that this component was redundant for the modeling. These differences were again attributed to the different sampling geometries. Since the reflection sampling geometry applied in this work favors shallow tissue layers, it is more likely to detect changes in skin composition associated with inflammation.[11] The more pronounced increase in muscular tissue transmission signal for sCAIA mice (Figure 5A) was attributed to the formation of pannus in the tibiotarsal and metatarsal regions. Comparing the library spectrum of muscle and the average of spectra collected from pannus *ex vivo* using Raman micro-spectroscopy revealed very similar spectral features (Figure 5C). Even though the contribution from muscle for the sCAIA group follows a distinctively different tendency compared to the asCAIA and control groups, sCAIA mice were not statistically different from the controls at day 13 (Figure 5A). However, this was clearly the case at day 10 (Kruskal–Wallis test $p < 0.001$, Dunnet's test $p < 0.001$) and may therefore be attributed to the relatively low number of spectral observations from limbs with arthritis (sCAIA group, $n = 7$) making statistical analysis very sensitive to random variations induced during measurements. Based on statistical significance at day 13, the library-based fitting of reflection mode spectra suggested that this sampling geometry captured the most diverse tissue changes associated with induced arthritis. However, from both MTMR calculations and library-based fitting, transmission mode performed slightly better for monitoring changes to bone and pannus formation. The time resolved quantitative analysis presented in this work is subject to relatively large standard deviations, suggesting that some attention must be given to refining the technique and experimental procedure. Nevertheless, general trends in the dynamics across groups can be observed, with almost all cases showing that arthritis mice are subject to changes in tissue composition that are statistically different from the control group and mice without arthritis. Given the continuous effort in development of improved antiarthritic therapeutics[8] and the importance of rodent preclinical animal models[3,4] there is a need for novel methods that can refine and reduce the use of animals in research.[7−9] The ability to follow disease-mediated tissue alterations *in vivo*, non-destructively, beyond the usual measures of apatite, could lead to novel biomarkers that are more efficient in reporting drug efficacy. This in turn could lead to reducing the duration of animal experiments and suffering. The method devised herein is readily capable of reporting on bone conditions and soft tissue simultaneously without involving ionizing radiation. In addition, the technique offers an objective readout, unlike conventional non-invasive readouts of arthritis severity based on clinical grading.[8,49]

■ CONCLUSIONS

Raman spectroscopy offers a novel approach for non-invasive and quantitative monitoring of disease progression in rodent models of inflammatory arthritis.

Using a combined transmission and reflection Raman spectroscopy system, we collected spectra from the tibiotarsal region of mice induced with and without arthritis over the course of 2 weeks. We took advantage of the ability to extract biomolecular information of soft and mineralized tissue simultaneously to produce longitudinally resolved quantifications of the major tissue components: bone, lipids, muscle, tendon, and skin. In general, these were subject to significant changes associated with disease in mice with arthritis compared to controls. The spectroscopic findings were compared with histology and μCT. A strong correlation of Raman-derived measures of tissue mineral content with tomography-derived bone density was obtained. The technique presented herein allows for objective repeated within animal measurements, potentially refining and reducing the use of animals in research while improving the development of novel antiarthritic therapeutics.

■ ASSOCIATED CONTENT

Data Availability Statement

The data underlying this study will be made available upon publication at https://github.com/MartinABHedegaard/CAIA

https://doi.org/10.1021/acs.analchem.2c04743
Anal. Chem. 2023, 95, 3720−3728

Supporting Information

The Supporting Information is available free of charge at https://pubs.acs.org/doi/10.1021/acs.analchem.2c04743.

Experimental details, arthritis scores, histology micrographs, μCT images, mineral-to-matrix ratios, and volumetric bone mineral densities and related comments (PDF)

AUTHOR INFORMATION

Corresponding Authors

Mads S. Bergholt − *Centre for Craniofacial and Regenerative Biology, King's College London, SE1 9RT London, UK;* orcid.org/0000-0003-3986-8942; Email: mads.bergholt@kcl.ac.uk

Martin A. B. Hedegaard − *SDU Chemical Engineering, University of Southern Denmark, 5230 Odense, Denmark;* Email: marhe@igt.sdu.dk

Authors

Anders R. Walther − *SDU Chemical Engineering, University of Southern Denmark, 5230 Odense, Denmark;* orcid.org/0000-0003-4940-2644

Elzbieta Stepula − *Centre for Craniofacial and Regenerative Biology, King's College London, SE1 9RT London, UK;* orcid.org/0000-0002-9243-9496

Nicholas Ditzel − *Molecular Endocrinology Unit (KMEB), Department of Endocrinology, Odense University Hospital and University of Southern Denmark, 5000 Odense, Denmark*

Moustapha Kassem − *Molecular Endocrinology Unit (KMEB), Department of Endocrinology, Odense University Hospital and University of Southern Denmark, 5000 Odense, Denmark*

Complete contact information is available at: https://pubs.acs.org/10.1021/acs.analchem.2c04743

Author Contributions

A.R.W. and E.S. contributed equally. The manuscript was written through contributions of all authors. All authors have given their approval to the final version of the manuscript. A.R.W: conceptualization, investigation, formal analysis, visualization, writing—original draft, writing review and editing. E.S: conceptualization, investigation, writing—review and editing. N.D: investigation, resources, formal analysis. M.K: resources, writing—review and editing. M.S.B and M.A.B.H: conceptualization, resources, writing—review and editing, funding acquisition, project administration, supervision.

Notes

The authors declare no competing financial interest.

ACKNOWLEDGMENTS

We thank the National Centre for the Replacement, Refinement and Reduction of Animals in Research (NC3Rs) for funding this work (NC/C018202/1 to M.A.B.H and M.S.B). This work was supported by Glaxo Smith Kline and Galvani Bioelectronics, with co-funding from the Engineering and Physical Sciences Research Council (EPSRC).

REFERENCES

(1) Firestein, G. S. *Nature* **2003**, *423*, 356−361.

(2) Picerno, V.; Ferro, F.; Adinolfi, A.; Valentini, E.; Tani, C.; Alunno, A. *Clin. Exp. Rheumatol.* **2015**, *33*, 551−558.

(3) Hegen, M.; Keith, J. C.; Collins, M.; Nickerson-Nutter, C. L. *Ann. Rheum. Dis.* **2008**, *67*, 1505−1515.

(4) Bolon, B.; Stolina, M.; King, C.; Middleton, S.; Gasser, J.; Zack, D.; Feige, U. *J. Biomed. Biotechnol.* **2011**, *2011*, 1−21.

(5) Hayer, S.; Vervoordeldonk, M. J.; Denis, M. C.; Armaka, M.; Hoffmann, M.; Bäcklund, J.; Nandakumar, K. S.; Niederreiter, B.; Geka, C.; Fischer, A.; Woodworth, N.; Blüml, S.; Kollias, G.; Holmdahl, R.; Apparailly, F.; Koenders, M. I. *Ann. Rheum. Dis.* **2021**, *80*, 714−726.

(6) Khachigian, L. M. *Nat. Protoc.* **2006**, *1*, 2512−2516.

(7) Hawkins, P.; Armstrong, R.; Boden, T.; Garside, P.; Knight, K.; Lilley, E.; Seed, M.; Wilkinson, M.; Williams, R. O. *Inflammopharmacology* **2015**, *23*, 131−150.

(8) Lim, M. A.; Louie, B.; Ford, D.; Heath, K.; Cha, P.; Betts-Lacroix, J.; Lum, P. Y.; Robertson, T. L.; Schaevitz, L. *Front. Pharmacol.* **2017**, *8*, 818.

(9) Marenzana, M.; Vande Velde, G. *Best Pract. Res. Clin. Rheumatol.* **2015**, *29*, 715−740.

(10) Schett, G.; Middleton, S.; Bolon, B.; Stolina, M.; Brown, H.; Zhu, L.; Pretorius, J.; Zack, D. J.; Kostenuik, P.; Feige, U. *Arthritis Rheum.* **2005**, *52*, 1604−1611.

(11) Lee, S. W.; Greve, J. M.; Leaffer, D.; Lollini, L.; Bailey, P.; Gold, G. E.; Biswal, S. *NMR Biomed.* **2008**, *21*, 527−536.

(12) Bhatnagar, S.; Khera, E.; Liao, J.; Eniola, V.; Hu, Y.; Smith, D. E.; Thurber, G. M. *Sci. Rep.* **2019**, *9*, 4661.

(13) Jermyn, M.; Desroches, J.; Aubertin, K.; St-Arnaud, K.; Madore, W. J.; De Montigny, E.; Guiot, M. C.; Trudel, D.; Wilson, B. C.; Petrecca, K.; Leblond, F. *Phys. Med. Biol.* **2016**, *61*, R370−R400.

(14) Hosu, C. D.; Moisoiu, V.; Stefancu, A.; Antonescu, E.; Leopold, L. F.; Leopold, N.; Fodor, D. *Laser Med. Sci.* **2019**, *34*, 827−834.

(15) Santos, I. P.; Barroso, E. M.; Bakker Schut, T. C.; Caspers, P. J.; van Lanschot, C. G. F.; Choi, D. H.; van der Kamp, M. F.; Smits, R. W. H.; van Doorn, R.; Verdijk, R. M.; Noordhoek Hegt, V.; von der Thüsen, J. H.; van Deurzen, C. H. M.; Koppert, L. B.; van Leenders, G. J. L. H.; Ewing-Graham, P. C.; van Doorn, H. C.; Dirven, C. M. F.; Busstra, M. B.; Hardillo, J.; Sewnaik, A.; ten Hove, I.; Mast, H.; Monserez, D. A.; Meeuwis, C.; Nijsten, T.; Wolvius, E. B.; Baatenburg de Jong, R. J.; Puppels, G. J.; Koljenović, S. *Analyst* **2017**, *142*, 3025−3047.

(16) Shu, C.; Chen, K.; Lynch, M.; Maher, J. R.; Awad, H. A.; Berger, A. *J. Biomed. Opt. Express* **2018**, *9*, 4781.

(17) Pavlou, E.; Zhang, X.; Wang, J.; Kourkoumelis, N. *Ann. Jt.* **2018**, *3*, 83.

(18) Das Gupta, S.; Finnilä, M. A. J.; Karhula, S. S.; Kauppinen, S.; Joukainen, A.; Kröger, H.; Korhonen, R. K.; Thambyah, A.; Rieppo, L.; Saarakkala, S. *Acta Biomater.* **2020**, *106*, 145−155.

(19) Jensen, M.; Horgan, C. C.; Vercauteren, T.; Albro, M. B.; Bergholt, M. S. *Opt. Lett.* **2020**, *45*, 2890.

(20) Carvalho, C. S.; Martin, A. A.; Santo, A. M. E.; Andrade, L. E. C.; Pinheiro, M. M.; Cardoso, M. A. G.; Raniero, L. *Theor. Chem. Acc.* **2011**, *130*, 1211−1220.

(21) Chaudhary, N.; Nguyen, T. N. Q.; Ahmad, M.; Harrington, R.; Jefferies, C. A.; Kearns, G.; Meade, A. D.; Wynne, C. *Clin. Spectrosc.* **2021**, *3*, 100009.

(22) Stevens, O.; Iping Petterson, I. E.; Day, J. C. C.; Stone, N. *Chem. Soc. Rev.* **2016**, *45*, 1919−1934.

(23) Schulmerich, M. V.; Cole, J. H.; Kreider, J. M.; Esmonde-White, F.; Dooley, K. A.; Goldstein, S. A.; Morris, M. D. *Appl. Spectrosc.* **2009**, *63*, 286−295.

(24) Khmaladze, A.; Kuo, S.; Kim, R. Y.; Matthews, R. V.; Marcelo, C. L.; Feinberg, S. E.; Morris, M. D. *Tissue Eng., Part C* **2015**, *21*, 46−51.

(25) Walther, A. R.; Ditzel, N.; Kassem, M.; Andersen, M. Ø.; Hedegaard, M. A. B. *Biomater. Biosyst.* **2022**, *7*, 100059.

(26) du Sert, N. P.; Ahluwalia, A.; Alam, S.; Avey, M. T.; Baker, M.; Browne, W. J.; Clark, A.; Cuthill, I. C.; Dirnagl, U.; Emerson, M.; Garner, P.; Holgate, S. T.; Howells, D. W.; Hurst, V.; Karp, N. A.; Lazic, S. E.; Lidster, K.; MacCallum, C. J.; Macleod, M.; Pearl, E. J.; Petersen, O. H.; Rawle, F.; Reynolds, P.; Rooney, K.; Sena, E. S.;

Silberberg, S. D.; Steckler, T.; Würbel, H. *PLoS Biol.* **2020**, *18*, No. e3000411.
(27) Hutamekalin, P.; Saito, T.; Yamaki, K.; Mizutani, N.; Brand, D. D.; Waritani, T.; Terato, K.; Yoshino, S. *J. Immunol. Methods* **2009**, *343*, 49−55.
(28) Nandakumar, K. S.; Svensson, L.; Holmdahl, R. *Am. J. Pathol.* **2003**, *163*, 1827−1837.
(29) Purvis, K.; Cisek, R.; Tokarz, D. *J. Chem. Educ.* **2019**, *96*, 1977−1981.
(30) Ito, Y.; Kennan, R. P.; Watanabe, E.; Koizumi, H. *J. Biomed. Opt.* **2000**, *5*, 383.
(31) Eilers, P. H. C. *Anal. Chem.* **2003**, *75*, 3631−3636.
(32) Eilers, P. H. C.; Boelens, H. F. M. *Baseline Correction with Assymmetric Least Squares Smoothing*; Leiden University Medical Centre Report, 2005.
(33) Zhang, D.; Jallad, K. N.; Ben-Amotz, D. *Appl. Spectrosc.* **2001**, *55*, 1523−1531.
(34) Mandair, G. S.; Morris, M. D. *BoneKEy Rep.* **2015**, *4*, 4.
(35) Bergholt, M. S.; Zheng, W.; Lin, K.; Ho, K. Y.; Teh, M.; Yeoh, K. G.; So, J. B. Y.; Huang, Z. *J. Biomed. Opt.* **2011**, *16*, 037003.
(36) Maher, J. R.; Inzana, J. A.; Awad, H. A.; Berger, A. J. *J. Biomed. Opt.* **2013**, *18*, 077001.
(37) Rygula, A.; Majzner, K.; Marzec, K. M.; Kaczor, A.; Pilarczyk, M.; Baranska, M. *J. Raman Spectrosc.* **2013**, *44*, 1061−1076.
(38) De Gelder, J.; De Gussem, K.; Vandenabeele, P.; Moens, L. *J. Raman Spectrosc.* **2007**, *38*, 1133−1147.
(39) Czamara, K.; Majzner, K.; Pacia, M. Z.; Kochan, K.; Kaczor, A.; Baranska, M. *J. Raman Spectrosc.* **2015**, *46*, 4−20.
(40) Movasaghi, Z.; Rehman, S.; Rehman, I. U. *Appl. Spectrosc. Rev.* **2007**, *42*, 493−541.
(41) Huang, N.; Short, M.; Zhao, J.; Wang, H.; Lui, H.; Korbelik, M.; Zeng, H. *Opt. Express* **2011**, *19*, 22892.
(42) Walther, A. R.; Andersen, M. Ø.; Dam, C. K.; Karlsson, F.; Hedegaard, M. A. B. *Appl. Spectrosc.* **2020**, *74*, 88−96.
(43) Matousek, P.; Stone, N. J. *Biophotonics* **2013**, *6*, 7−19.
(44) Grahnemo, L.; Andersson, A.; Nurkkala-Karlsson, M.; Stubelius, A.; Lagerquist, M. K.; Svensson, M. N. D.; Ohlsson, C.; Carlsten, H.; Islander, U. *Arthritis Res. Ther.* **2015**, *17*, 189.
(45) Halloran, B. P.; Ferguson, V. L.; Simske, S. J.; Burghardt, A.; Venton, L. L.; Majumdar, S. J. *Bone Miner. Res.* **2002**, *17*, 1044−1050.
(46) Richbourg, H. A.; Martin, M. J.; Schachner, E. R.; McNulty, M. A. *Anat. Rec.* **2017**, *300*, 450−459.
(47) Papageorgiou, M.; Föger-Samwald, U.; Wahl, K.; Kerschan-Schindl, K.; Pietschmann, P. *Calcif. Tissue Int.* **2020**, *106*, 431−443.
(48) Chao, C. C.; Chen, S. J.; Adamopoulos, I. E.; Judo, M.; Asio, A.; Ayanoglu, G.; Bowman, E. P. *Autoimmunity* **2010**, *43*, 642−653.
(49) Perilli, E.; Cantley, M.; Marino, V.; Crotti, T. N.; Smith, M. D.; Haynes, D. R.; Dharmapatni, A. A. S. S. K. *Scand. J. Immunol.* **2015**, *81*, 142−150.

https://doi.org/10.1021/acs.analchem.2c04743
Anal. Chem. 2023, 95, 3720−3728